*Eleventh International Conference on CFD in the Minerals and Process Industries*
*CSIRO, Melbourne, Australia*
*7-9 December 2015*

# DEM-CFD COUPLING: MATHEMATICAL MODELLING AND CASE STUDIES USING ROCKY-DEM® AND ANSYS FLUENT®

**Clarissa B. FONTE[1], João A. A. OLIVEIRA Jr. [1] and Lucilla C. de ALMEIDA[1*]**

[1] Engineering Simulation and Scientific Software, Rio de Janeiro, BRAZIL
*Corresponding author, E-mail address: lucilla@esss.com.br

## ABSTRACT

Coupling between Discrete Element Modelling (DEM) and Computational Fluid Dynamics (CFD) packages is a promising approach to model granular-fluid systems, enlarging the range of particle-fluid processes that can be managed with numerical simulation.

In this paper, coupling approach for the commercial software packages Rocky® (DEM) and ANSYS Fluent® (CFD) will be addressed. Rocky® is a powerful DEM software that can handle true non-round particle shapes, breakage, physical wear and is efficient on both CPU and GPU systems, among other capabilities. ANSYS Fluent® package is well known as one of the world leaders for CFD applications.

Mathematical modelling for DEM, CFD and the coupling itself will be described, as well as two case studies. The first one is a one-way coupling case, meaning that only the fluid flow affects the particle movement. This example demonstrates the method capability of considering the effect of drag force on the particles. Also, the importance of choosing a suitable drag law for the case is made clear. The second study considers a dense flow, and therefore two-way coupling, in which both phases have an influence in each other, is demonstrated. Comparison with experimental data proves the capability of the fluid also being influenced by a reactive force.

## NOMENCLATURE

| | |
|---|---|
| $C_D$ | drag coefficient |
| $d_p$ | particle equivalent diameter |
| $d'_p$ | diameter of a sphere which has its projected area (in the direction of the flow) equal to the actual particle projected area |
| $ds_n$ | change in normal contact overlap during time step |
| $ds_t$ | tangential particle displacement during time step |
| $D$ | pipe diameter |
| $E_p$ | particle material loading stiffness |
| $E_b$ | boundary material loading stiffness |
| $\mathbf{F}_D$ | drag force |
| $\mathbf{F}_p^C$ | contact forces on the particle |
| $\mathbf{F}_{p,n}^C$ | normal elastic-plastic contact force on the particle |
| $\mathbf{F}_{p,n}^{C,t}$ | normal elastic-plastic contact force on the particle at current time step |
| $\mathbf{F}_{p,n}^{C,t-dt}$ | normal elastic-plastic contact force on the particle at previous time step |
| $\mathbf{F}_{p,t}^C$ | tangential contact force on the particle |
| $\mathbf{F}_{p,t}^{C,t}$ | tangential contact force on the particle at current time step |
| $\mathbf{F}_{p,t}^{C,t-dt}$ | tangential contact force on the particle at previous time step |
| $\mathbf{F}_p^{fp}$ | fluid-particle interaction forces on the particle |
| $\mathbf{F}_f^{pf}$ | fluid-particle interaction forces on the fluid |
| $F_{\nabla p}$ | pressure gradient force |
| $\mathbf{g}$ | gravitational acceleration |
| $\mathbf{I}_p$ | particle moment of inertia tensor |
| $K_1$ | Stokes form factor |
| $K_2$ | Newton form factor |
| $K_{nl}$ | contact stiffness for loading parts |
| $K_{nbl}$ | boundary loading stiffness |
| $K_{npl}$ | particle loading stiffness |
| $K_{nu}$ | contact stiffness for unloading parts |
| $L_p$ | particle size |
| $m_p$ | particle mass |
| $p$ | pressure |
| $Re$ | relative Reynolds number |
| $s_n^t$ | normal overlap at current time step |
| $s_n^{t-dt}$ | normal overlap at previous time step |
| $t$ | time |
| $\mathbf{T}_p$ | torque on the particle |
| $\mathbf{u}$ | fluid velocity |
| $\mathbf{v}$ | translational particle velocity |
| $V_{cell}$ | cell volume |
| $V_p$ | particle volume |
| $\alpha_f$ | fluid volume fraction |
| $\varepsilon$ | coefficient of restitution |
| $\mu_d$ | dynamic friction coefficient |
| $\mu_f$ | fluid viscosity |
| $\mu_s$ | static friction coefficient |
| $\rho_f$ | fluid density |
| $\boldsymbol{\tau}_f$ | viscous stress tensor |
| $\phi$ | particle sphericity |
| $\Psi$ | blending function |
| $\boldsymbol{\omega}_p$ | particle angular velocity |

## INTRODUCTION

Discrete Element Method (DEM) is a numerical technique that deals with granular flows, which consist of a large number of solid particles (such as sand, ore, grain, among others). Derivation of continuous equations of state and motion for this type of media is complicated and, thus, DEM aims to solve these problems by the simulation of the evolution of every particle in the system subject to contact forces. Instead of numerical integration of the continuum equations of motion and state, the motion of each particle is simulated, as well as the interaction for each particle-particle and particle-boundary pair.

Computational Fluid Dynamics (CFD) predicts fluid flow, heat and mass transfer by solving equations of conservation of mass, momentum, energy and species. Other related phenomena, such as chemical reactions and combustion, can be accounted for if necessary.

The coupled DEM-CFD approach is a promising alternative for modelling granular-fluid systems. Being able to deal with flows with high solids concentrations, this coupling enlarges the range of particle-fluid processes that can be managed with numerical simulations. Complex phenomena such as pneumatic conveying, granular drying, slurry flow inside grinding mills or even chemical reactions between particles and fluids can be handled with these powerful tools.

Introduced by early developers such as Hoomans *et al.* (1996), Tsuji *et al.* (1993) and Xu and Yu (1997), DEM-CFD coupling models the motion of particles as a discrete phase, whereas the fluid flow is treated as a continuous phase described by the local volume averaged Navier-Stokes equations (VANS) on a computational cell scale (Drew, 1983). This approach has been recognized as an effective method to study the fundamentals of particle–fluid flow by various investigators (Zhu *et al.*, 2008).

There are two ways to couple DEM and CFD technologies: one-way coupling, in which only the fluid flow affects the particle movement, and two-way coupling, in which the particle flow also influences the continuous phase behaviour.

In this paper, coupling between DEM package Rocky® and CFD package ANSYS Fluent® will be demonstrated. Rocky® is a DEM software capable of performing 3D simulations of granular flows. It uses real particle geometries and analyses aspects such as 3D surface wear modification, particle breakage, sticky particles, as well as rotating and vibrating boundaries. ANSYS Fluent® package is a well established software for CFD applications.

Both DEM and CFD techniques can present high computational costs depending on the system being simulated. However, one can overcome this by using adequate computational equipment. Rocky® can run in parallel, both under a CPU or a GPU cluster system. ANSYS Fluent®, in its turn, has a well documented HPC CPU capability. These capabilities are useful when dealing with problems of increasing complexity.

## MODEL DESCRIPTION

This section will provide a brief description of DEM, CFD and coupling methods.

### DEM MODELLING

Granular material flows can behave similar to solids or fluids. This behaviour leads to substantial difficulties for modelling this kind of flows using continuous equations of state and motion.

Considering this, DEM is an important alternative for handling these flows numerically, since it is a technique that simulates the motion of every particle in a granular matter.

All particles within the computational domain are tracked in a Lagrangian way, explicitly solving Newton's second law that governs translational (equation 1) and rotational (equation 2) particle motion. For further information see Guo and Curtis (2014).

$$m_p \frac{d\mathbf{v}_p}{dt} = \mathbf{F}_p^C + m_p\mathbf{g} + \mathbf{F}_p^{\mathrm{fp}} \quad (1)$$

$$\mathbf{I}_p \frac{d\boldsymbol{\omega}_p}{dt} = \mathbf{T}_p \quad (2)$$

It is clear from the equations above that forces acting on each particle must be calculated. Generally, these forces can be divided into two categories: contact forces (for every particle-particle and particle-boundary interaction) and other forces, such as body forces or fluid forces (if fluid is considered in the simulation).

In general, contact forces can be decomposed into two orthogonal components, consisting of forces normal and tangential to the contact plane, as can be seen in equation 3:

$$\mathbf{F}_p^C = \mathbf{F}_{p,n}^C + \mathbf{F}_{p,t}^C \quad (3)$$

In a DEM code, particles are usually not deformable, but are allowed to slightly overlap, as illustrated by figure 1. Normal and tangential directions are defined as a function of normal overlap and tangential relative particle displacement as seen in the models described in the following sections.

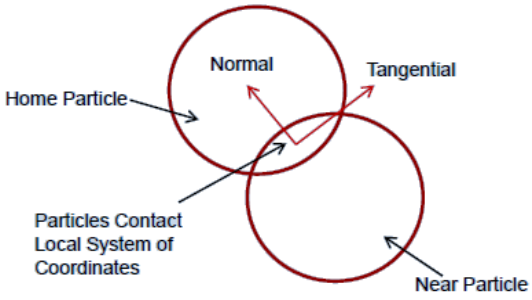


**Figure 1**: Particle contact forces considering overlapping particles.

Models for these forces implemented in Rocky® are presented in the following sections.

#### *Normal contact forces*

Linear hysteresis is an elastic-plastic model that allows the simulation of plastic energy dissipation on a contact with the advantage of not incurring in large simulation times. Other advantages are that contact energy dissipation is not sensitive to other contacts, force is zero at zero contact deformation as expected, energy dissipation does not depend on loading rate and the coefficient of restitution is velocity independent. On the other hand, contact force and overlap history has to be retained, which makes it more difficult to implement.

In this model, the shape of overlap-normal force is approximated by two straight lines of different slopes, one for loading and other for unloading, as illustrated on figure 2 for a collision of a 100 mm particle on a flat plate. This normal force is calculated in Rocky® by equations 4 to 6 (Walton, 1993).

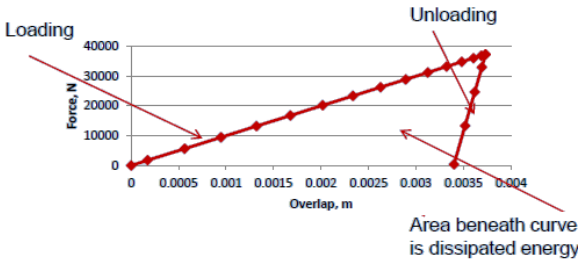


**Figure 2**: Normal force as obtained in a Rocky® simulation of a collision of 100 mm particle on a flat plate.

$$\mathbf{F}_{p,n}^{C,t} = \min\left(\mathbf{F}_{p,n}^{C,t-dt} + K_{nu} ds_n, K_{nl} s_n\right) \text{ if } ds_n \geq 0 \quad (4)$$

$$\mathbf{F}_{p,n}^{C,t} = \max\left(\mathbf{F}_{p,n}^{C,t-dt} + K_{nu} ds_n, 0.001 K_{nl} s_n\right) \text{ if } ds_n < 0 \quad (5)$$

$$ds_n = s_n^t - s_n^{t-dt} \quad (6)$$

In these equations, $K_{nl}$ and $K_{nu}$ are values of the contact stiffness for loading and unloading parts. The particle loading stiffness, $K_{npl}$, is calculated as:

$$K_{npl} = E_p L_p \quad (7)$$

For the contact of particle and boundary, the equation is similar. However, instead of particle material loading stiffness, $E_p$, boundary material loading stiffness, $E_b$, is used. Boundary loading stiffness, $K_{nbl}$, is thus calculated as:

$$K_{nbl} = E_b L_p \quad (8)$$

Therefore, for the contact of two particles, loading stiffnesses are defined as:

$$K_{nl} = \frac{K_{npl,1} \cdot K_{npl,2}}{K_{npl,1} + K_{npl,2}} \quad (9)$$

$$K_{nu} = \frac{K_{nl}}{\varepsilon^2} \quad (10)$$

In equation 9, 1 and 2 refer to different particles. In case of particles against boundary contact, the equations for loading and unloading stiffness become:

$$K_{nl} = \frac{K_{npl} \cdot K_{nbl}}{K_{npl} + K_{nbl}} \quad (11)$$

$$K_{nu} = \frac{K_{nl}}{\varepsilon^2} \quad (12)$$

This model is appropriate for flow of non-adhesive materials. For cases involving adhesive materials, other models implemented in Rocky® are more suitable. However, those will not be discussed in this paper.

### *Tangential contact forces*

Linear elastic-frictional model is used. This model has simple elastic behaviour before onset of friction and can reproduce Coulomb frictional contact behaviour for static and dynamic frictional values. However, contact force and displacement history has to be retained, which makes this model more difficult to implement.

If no sliding is taking place for the contact, the equation below is considered for tangential force:

$$\mathbf{F}_{p,t}^{C,t} = \min\left(\mathbf{F}_{p,t}^{C,t-dt} + K_{nl} ds_t, \mu_s \mathbf{F}_n^{C,t}\right) \quad (13)$$

If sliding is taking place for the contact, then the equation below is used:

$$\mathbf{F}_{p,t}^{C,t} = \min\left(\mathbf{F}_{p,t}^{C,t-dt} + K_{nl} ds_t, \mu_d \mathbf{F}_n^{C,t}\right) \quad (14)$$

It is considered that sliding takes place on the contact when tangential force exceeds the limit of $\mu_s \mathbf{F}_n^{C,t}$. Once tangential force falls below the value of $\mu_d \mathbf{F}_n^{C,t}$, the contact is considered non-sliding again.

## CFD MODELLING

A large number of researchers carried out studies to achieve basic understanding of the complex flows involving multiphase systems during past years. Basic equations are usually formulated using volume or ensemble methods (Vasquez and Ivanov, 2000). Derivation of basic multiphase flow equations and different averaging methods can be found in Ishii (1975), Drew (1983), Soo (1990) and Gidaspow (1993).

In this work, the classical Navier-Stokes equations are modified and averaged in volume (Drew, 1983), returning the same expressions obtained with the two-fluid model equations unless only one phase is considered. This enables the usage of ANSYS Fluent® solver in this coupling implementation with Rocky®.

The averaged mass and momentum conservation equations are written as:

$$\frac{\partial}{\partial t}\left(\alpha_f \rho_f\right) + \nabla \cdot \left(\alpha_f \rho_f \mathbf{u}\right) = 0 \quad (15)$$

$$\frac{\partial}{\partial t}\left(\alpha_f \rho_f \mathbf{u}_f\right) + \nabla \cdot \left(\alpha_f \rho_f \mathbf{u}\mathbf{u}\right) = -\alpha_f \nabla p + \alpha_f \nabla \cdot \boldsymbol{\tau}_f + \alpha_f \rho_f \mathbf{g} - \mathbf{F}_f^{pf} \quad (16)$$

To solve this set of equations, ANSYS Fluent® is used. ANSYS Fluent® is a finite volume, cell-centred code which uses an implicit scheme for time stepping. A block algebraic multigrid solver is used for the solution of the linearized equations (Hutchinson and Raithby, 1986). The PC-SIMPLE algorithm, which is the SIMPLE algorithm extended to multiphase flows, is used for the pressure-velocity coupling. More detailed information about this coupling segregated pressure-based method can be found in Vasquez and Ivanov, 2000.

A source term is included on the disperse phase continuity equation to impose the disperse volume fraction calculated at the DEM side. The secondary phase momentum equations are not solved by ANSYS Fluent®, as the dispersed phase velocity comes from the DEM solver. The momentum exchange term is not calculated in the CFD solver, but in DEM side, as explained in the next section, and included in the formulation through a source term in the continuous phase momentum equation.

## DEM-CFD COUPLING MODELLING

The influence of the fluid flow on the particle motion is achieved by the $\mathbf{F}_p^{fp}$ term in equation 1. This term sums up all the fluid forces acting on the particle, such as drag and pressure forces, as well as non-drag forces like virtual mass force, Basset force, lift force, Saffman and Magnum forces (due to particle rotation), Van der Waals force, cohesive forces, among others. Depending on the flow conditions, most of these forces can be neglected. In this

study, only drag and pressure gradient forces are considered.

Pressure gradient force is given by:

$$\mathbf{F}_{\nabla P} = -V_p \nabla p \tag{17}$$

Drag force is calculated as:

$$\mathbf{F}_D = \beta(\mathbf{u} - \mathbf{v}) \tag{18}$$

Drag force exerted on a single particle is different from drag force on a particle surrounded by others. Therefore, β is a coefficient that depends on the volume fraction of the cell where the drag is computed as well as the drag coefficient, as can be seen in the following equation.

$$\beta = \frac{3}{4}\frac{(1-\alpha_f)\rho_f C_D}{d_p}|\mathbf{v} - \mathbf{u}| \tag{19}$$

In this coupling, various drag correlations are available based on particle type (spherical or non-spherical) and particle concentration (dilute flows or dense flows). Here, three of them, which are used in the examples in the next sections, will be discussed.

The first of them is Schiller and Naumann correlation, which is well suited for spherical particles and dilute flows. For more details see Crowe *et al.* (2012). The modified correlation, which increases the valid range of relative Reynolds number so that inertial drag range is also covered (*Re* >1000), is considered:

$$C_D = \max\left[\frac{24}{\mathrm{Re}}\left(1 + 0.15\,\mathrm{Re}^{0.687}\right), 0.44\right] \tag{20}$$

Relative particle Reynolds number is defined as:

$$\mathrm{Re} = \frac{\rho_F |\mathbf{v} - \mathbf{u}| d_P}{\mu_F} \tag{21}$$

Ganser (1993) correlation is suited for spherical and non-spherical particles and dilute flows. It relates the drag over a particle with the Stokes form factor, $K_1$, the Newton form factor, $K_2$, and the particle relative Reynolds number, *Re*. Ganser correlation, as well as the form factors, appear below:

$$\frac{C_D}{K_2} = \frac{24}{\mathrm{Re}\,K_1 K_2}\left[1 + 0.1118(\mathrm{Re}\,K_1 K_2)^{0.6567}\right] + \frac{0.4305}{1 + \frac{3305}{\mathrm{Re}\,K_1 K_2}} \tag{22}$$

$$K_1 = \left(\frac{1}{3}\frac{d_p'}{d_p} + \frac{2}{3}\phi^{-1/2}\right)^{-1} - 2.25\frac{d_p}{D} \tag{23}$$

$$K_2 = 10^{1.8148(-\log_{10}\phi)^{0.5743}} \tag{24}$$

Stokes factor is a function of $d'_p$, which represents the diameter of a sphere which has its projected area (in the direction of the flow) equal to the actual particle projected area (also in the direction of the flow). It is also important to notice that D is the diameter of the pipe where the flow occurs. Ganser correlation is valid for $ReK_1K_2 \leq 10^5$.

For a relatively low particle concentration ($\alpha_p < 0.2$), Wen and Yu developed a drag law correlation based on a series of experiments on fluidized beds (for more information see Gidaspow, 1993). This correlation is presented in terms of a correction (based on fluid volume fraction) of the Schiller and Naumann correlation, using a superficial velocity relative particle Reynolds number. For higher solids volume fractions, Wen and Yu drag law deviates from the experimental data. For these cases, with solids volume fraction from $\alpha_p \geq 0.2$ up to maximum packing limit, Ergun (1952) has developed a correlation to the head loss in fixed beds.

To make the transition between the Wen and Yu and Ergun correlations in a smooth way, Huilin and Guidaspow (2003) have applied a blending function to promote a link based on fluid volume fraction. The final drag correlation obtained is given by the following set of equations:

$$C_{D,H\&G} = \psi C_{D,Ergun} + (1-\psi)C_{D,W\&Y} \tag{25}$$

$$C_{D,W\&Y} = \begin{cases} \frac{24}{\alpha_f\,\mathrm{Re}}\left[1 + 0.15(\alpha_f\,\mathrm{Re})^{0.687}\right]\alpha_f^{-1.65} & \alpha_f\,\mathrm{Re} < 1000 \\ 0.44\alpha_f^{-1.65} & \alpha_f\,\mathrm{Re} < 1000 \end{cases} \tag{26}$$

$$C_{D,Ergun} = 200\frac{(1-\alpha_f)}{\alpha_f \phi^2\,\mathrm{Re}} + \frac{7}{3\phi} \tag{27}$$

Ψ is a blending function defined as:

$$\psi = \frac{\arctan\left(150 \cdot 1.75\left(0.8 - \alpha_f\right)\right)}{\pi} + 0.5 \tag{28}$$

The influence of the particles on the fluid flow is taken into account not only through the volume fraction in the VANS equations, but also through the force $\mathbf{F}_p^{fp}$ in equation 16. A semi-implicit treatment of the reactive force is adopted and the momentum exchange with the particulate phase is calculated as:

$$\mathbf{F}_f^{pf} = \frac{\sum_{p=1}^{N} \mathbf{F}_p^{fp}}{V_{cell}} \tag{29}$$

## WINDSHIFTER SIMULATION

A windshifter is a device typically used in industrial waste processes to separate light from heavy particles. It basically consists of a vertical shaft in which air stream flows upwards. Particles are dropped into the shaft and, depending on their sizes, shapes and densities, they rise or settle down.

The aim of this simulation was to compare the results when considering different drag laws. Since this case involves low discrete phase concentrations, one-way coupling was applied, which means that only fluid flow influences particle motion, and Schiller and Naumann and Ganser drag laws were compared.

In this example, Rocky®'s capabilities of modelling both spherical and non-spherical particles is used. The figure below shows the different geometries that are considered:

**Figure 3**: Geometries for paper (flat), stone (sphere), metal (rod) and wood (briquette), respectively.

An air inlet velocity of 20m/s was considered. The table below shows the information of the particles:

| Material | Shape | Sieve size (mm) | Density (kg/m$^3$) | Mass flow rate (kg/h) | Volume flow rate (m$^3$/h) |
|---|---|---|---|---|---|
| Paper | Flat | 20, 50, 80 | 800 | 1000 | 1,25 |
| Stone | Sphere | 20, 50, 80 | 3000 | 3750 | 1,25 |
| Metal | Rod | 20, 50, 80 | 8000 | 10000 | 1,25 |
| Wood | Briquette | 50 | 900 | 1125 | 1,25 |

**Table 1**: Particle information.

Following the workflow of a one-way coupling simulation, firstly, an ANSYS Fluent® analysis was carried out. A converged steady-state result for ANSYS Fluent® simulation is shown below. This simulation simply consists of air flowing through the shaft:

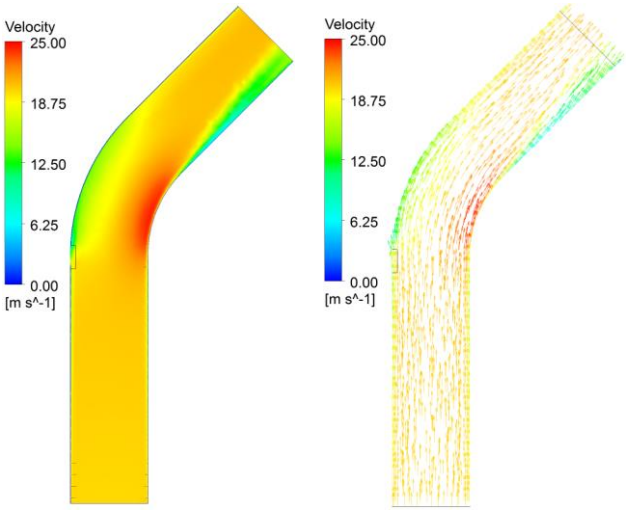


**Figure 4**: Velocity plot (left) and velocity vectors (right) for air flow through the shaft.

ANSYS Fluent® results were then exported to Rocky®. Figure 5 shows the results from DEM simulation in Rocky®, and the different behaviours that were obtained with different drag laws.

Schiller and Naumann drag law does not take into account non-sphericity of the particles, which leads to terminal velocity prediction higher than Ganser correlation. The Table 2 exemplifies terminal velocity calculation for paper (value of 0.434 for sphericity). It also indicates if the particle will rise or fall.

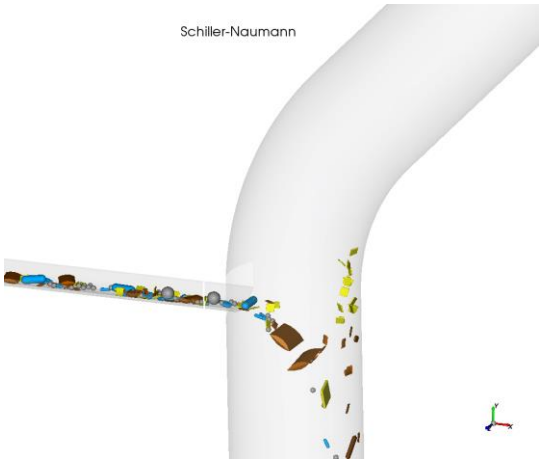


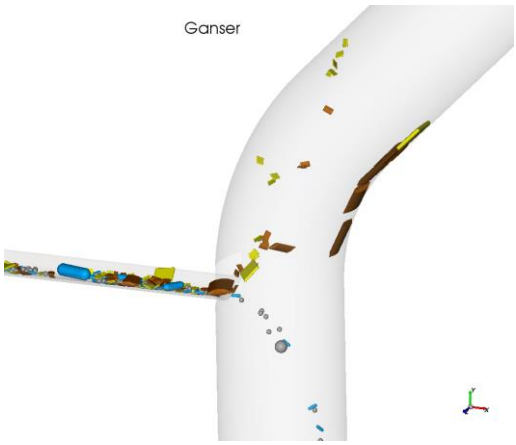


**Figure 5**: Schiller and Naumann and Ganser cases results. Different colours show different materials.

| Equivalent diameter (mm) | Terminal velocity (m/s) | |
|---|---|---|
| | Schiller & Naumann | Ganser |
| 2.0 | 19.69 | 7.71 |
| 5.0 | 31.13 | 12.31 |
| 8.0 | 39.38 | 15.66 |

**Table 2**: Terminal velocity calculation for paper.

As can be seen from figure 5 and Table 2, Schiller and Naumann correlation leads to higher terminal velocities and, consequently, a higher number of particles being collected at the bottom than expected, including paper particles. Ganser correlation, in its turn, gives more accurate results, since it considers particle geometry, which has an important influence on drag force. Figure 6 summarizes the results of overall collection at the bottom of the windshifter.

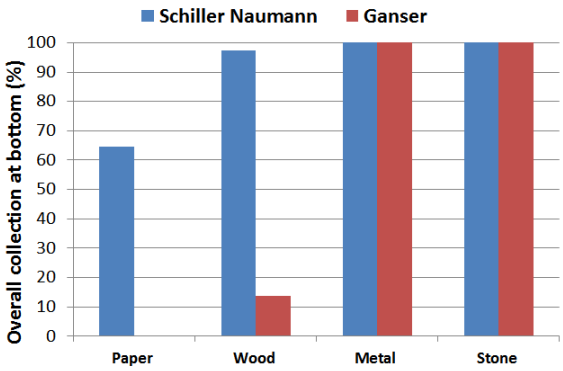


**Figure 6.** Overall collection at the bottom.

## FLUIDIZED BED SIMULATION

Fluidized beds are widely used in plant operations, mainly due to their good mixing characteristics and high contact surface area between gas and solid phases. Despite their widespread application, much of the development and design of fluidized bed reactors has been empirical, as the complex behaviour of gas–solid flow in these systems makes modelling a challenging task (Taghipour *et al.*, 2005). With the development of computational technology, numerical simulation method has been used to provide complete information in a granular flow (Liu et al., 2013).

This section will describe a fluidized bed case simulated using Rocky®-ANSYS Fluent® coupling. Since this problem involves high concentrations of solids, two-way coupling is considered, meaning that fluid and particle phases have an influence on each other. Also, Huilin and Gidaspow drag law was used.

The information for the case was published by USA's National Energy Technology Laboratory (NETL, 2013) and consists of a small scale fluidized bed. General conditions of the problem can be found in the table that follows:

| **Domain information** | |
|---|---|
| **Property** | **Value** |
| Domain size (W x D x H) (mm) | 23 x 8 x 123 |
| Grid cells (number of elements) | 24 x 8 x 124 |
| Pressure intake 1 y-distance (cm) | 4.13 |
| Pressure intake 2 y-distance (cm) | 34.61 |
| **Particle information – Group D Nylon beads (Spherical)** | |
| **Property** | **Value** |
| Sieve size (mm) | 3.256 |
| Density (kg/m$^3$) | 1131 |
| Mass of inventory (kg) | 1.90 |
| **Gas information** | |
| **Property** | **Value** |
| Density (kg/m$^3$) | 1.20 |
| Viscosity (Pa.s) | 1.9e-05 |
| Superficial velocity (m/s) | 2.18 |

**Table 3**: Domain and simulation set-up details.

The gas distributor was not included, so gas enters the domain through the bottom with uniform superficial velocity. Gas then leaves the domain through the top, which is under atmospheric conditions. A uniform grid with an initial bed composed by 92949 spherical particles with diameter of 3.256 mm and initial height of 16.4 cm was prescribed in the beginning of the simulation.

A uniform gas inlet was used, and velocity was prescribed in an increasing manner (from 0 m/s at t = 0s to case velocity at t = 2s), so that the beginning of the fluidization process could be observed. This strategy also provides more numerical stability. Standard k-ε turbulence model was applied.

Predicted pressure drop between inlet and outlet by Ergun's correlation was calculated for 3 different fluid volume fraction values (0.35, 0.4 and 0.45) for a range of fluid velocities. These curves are plotted as coloured dashed lines in figure 7.

It is important to point out that these curves are only valid until fluidization starts, which happens at the point where the minimum fluidization velocity curve (black dashed curve in figure 7), obtained by equating the pressure drop to the effective weight of the particles at the moment of incipient fluidization, crosses the pressure drop curve.

The simulated pressure drop between inlet and outlet versus the fluid superficial velocity is plotted in figure 7 as a continuous orange line. The agreement between the pressure drop predicted by Ergun's correlation and the pressure drop obtained in the simulation is fairly good until fluidization takes place.

The simulated pressure drop between the two pressure intake locations, as shown in table 3, is plotted in figure 8 and compared to the averaged pressure drop value obtained experimentally. In the same plot, the dashed line marks the moment in which the minimum fluidization velocity measured at experiments is achieved, and this quite coincides with the point in which the behaviour of the pressure drop changes from linear to constant in the simulation.

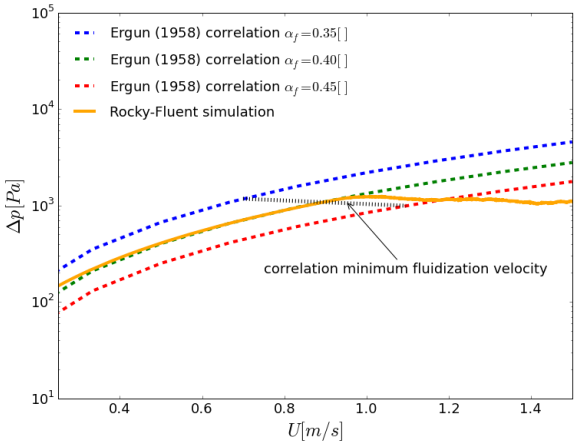


**Figure 7.** Pressure drop in fluidized bed case. Comparison between simulation and correlation results.

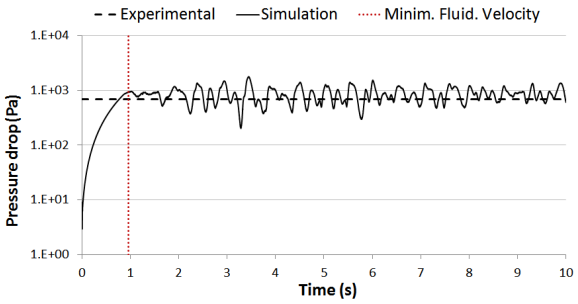


**Figure 8.** Pressure drop between the two pressure intake locations. Comparison between simulation and experimental results.

In order to observe the behaviour of the particles before and after fluidization starts, particles were divided into 7 different groups according to their initial position, as can be seen in figure 9(a), and these particle groups were then tracked during time. Figure 9(b) shows the moment in which fluidization is about to start and, as expected, the positions of the particles and bed height is nearly the same from initialization. Figure 9(c) shows the fluidization process with the gas superficial velocity gradually increasing, while figure 9(d) shows the location of the particles at the moment in which final velocity is achieved. The bubble formation when beyond minimum fluidization velocity can observed, confirming the expected bubbly regime, characteristic of fluidized beds operation. Figure 9(e) shows the increasing particle mixing and, lastly, figure 9(f) displays the particles configuration after 5s of simulation, showing that they are completely mixed, which confirms one of the main advantages of the industrial application of the fluidized bed concept.

## CONCLUSION

In this article, coupling between DEM and CFD packages Rocky® and ANSYS Fluent® was presented. Mathematical modelling was described, focusing on DEM, CFD and coupling methods.

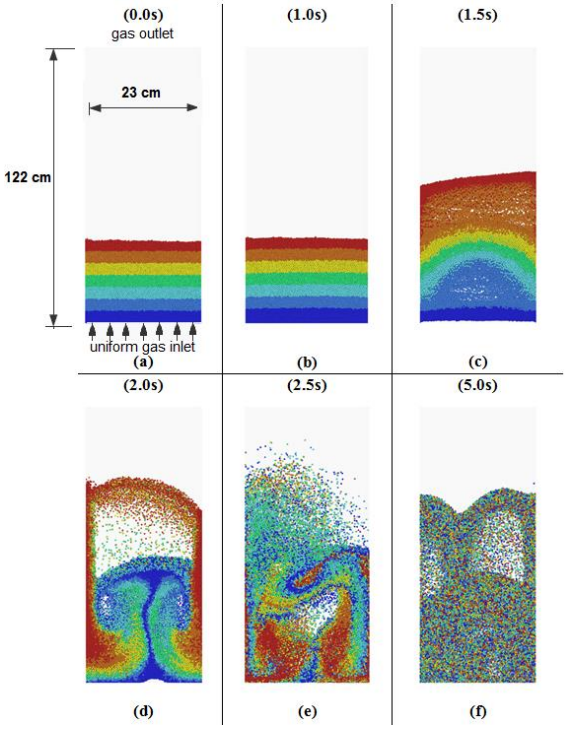


**Figure 9.** Evolution of particle behaviour with time. First figure shows the computational domain and fluid boundary conditions.

A windshifter simulation was presented in order to highlight one-way coupling results. The method capability of considering the effect of drag force on the particles was demonstrated, and the importance of choosing suitable drag laws was pointed out.

Also, a fluidized bed case, which consists of a dense flow example, was described. Two-way coupling was considered, showing good accordance to literature correlation, which states the capability of the fluid being affected by a reactive force.

Future developments for this coupling include implementation of non-drag laws, thermal fluid-particle coupling and mass exchange between fluid and particles.

## REFERENCES


ANSYS, Inc., (2013), "Fluent® Theory Guide", Cannonsbourg, PA, United States.

CROWE, C. T., SCHWARZKOPF, J. D., SOMMERFELD, M. and TSUJI, Y., (2012), "Multiphase Flows with Droplets and Particles", *CRC Pres.*, Boca Raton, FL, United States.

DREW, D., (1983), "Mathematical modelling of two-phase flow," *Annu. Rev. Fluid Mech*., **15**, 261-291.

ERGUN, S., (1952), "Fluid flow through packed columns", *Chem. Eng. Process*, **48**, 89–94.

GANSER, G. H., (1993), "A rational approach to drag prediction of spherical and non-spherical particles", *Powder Technology*, **77**, 143-152.

GIDASPOW, D., (1993), "Multiphase Flow and Fluidization: Continuum and Kinetic Theory Descriptions", *Academic Pres.*, San Diego, CA, United States.

GUO, Y. and CURTIS, J.S., (2014), "Discrete Element Method Simulations for Complex Granular Flows", *Annu. Rev. Fluid Mech.*, June 21-46.

HAIDER, A. and LEVENSPIEL, O., (1989), "Drag Coefficient and Terminal Velocity of Spherical and Non-spherical Particles", *Powder Technology*, **58**, 63-70.

HILTON, J.E., HILTON, L.R., MASON and CLEARY, P.W., (2010), "Dynamics of gas-solid fluidised beds with non-spherical particle geometry", *Chem Eng Science*., **65**, 1584-1596.

HOOMANS, B., KUIPERS, J., BRIELS, W. and VAN SWAAIJ, W., (1996), "Discrete particle simulation of bubble and slug formation in a two-dimensional gas-fluidized bed: a hard-sphere approach", *Chemical Engineering Science*, **60**, 99–118.

HUILIN, L. and GIDASPOW, D., (2003), "Hydrodynamics of binary Fluidization in a riser: CFD simulation using two granular temperatures", *Chemical Engineering Science*, **58**, 3777-3792.

HUTCHINSON, B., RAITHBY, G., (1986), "A Multigrid Method Based on the Additive Correction Strategy," *Numer. Heat Transfer*, **9**, 511-537.

ISHII, M., (1975), "Thermo-Fluid Dynamic Theory of Two-Phase Flow", Eyrolles, Paris.

LIU, G., ZANG, Y., LU, H., YOU, E. and LI, X., (2013), "Numerical Simulation of Particle Flow Motion in a Two-Dimensional Modular Pebble-Bed Reactor with Discrete Element Method" *Science and Technology of Nuclear Installations*.

National Energy Technology Laboratory, (2013), "NETL challenge problem: Small scale problem I", *https://mfix.netl.doe.gov/experimentation/challenge-problems.*

SOO, S., (1990), "Multiphase Fluid Dynamics", *Science Press*, Beijing, China.

TAGHUPOUR, F., ELLIS, N. and WONG, C., (2005) "Experimental and computational study of gas–solid fluidized bed hydrodynamics", *Chemical Engineering Science*, **60**, 6857-6867.

TSUJI, Y., KAWAGUCHI, T. and TANAKA, T., (1993), "Discrete particle simulation of two dimensional fluidized bed," *Powder Technol.*, **77**, 79–87.

VASQUEZ, S., IVANOV, V., (2000), "A Phase Coupled Method for Solving Multiphase Problems on Unstructured Meshes", *Proceeding of ASME FEDSM'00: ASME 2000 Fluids Engineering Division Summer Meeting*, Boston, MA, United States, June 11-15.

XU, B. and YU, A., (1997), "Numerical simulation of the gas–solid flow in a fluidized bed by combining discrete particle method with computational fluid dynamics," *Chemical Engineering Science*, **52**, 2785-2809.

WALTON, O., (1993), "Numerical simulation of inelastic, frictional particle-particle interactions". *Particulate Two-Phase Flow*, 884-911.

ZHU, H., ZHOU, Z., YANG, R. and YU, A., (2008), "Discrete particle simulation of particulate systems: a review of major applications and findings", *Chemical Engineering Science*, **63**, 5728–5770.